Ligand-channel-enabled ultrafast Li-ion conduction

https://doi.org/10.1038/s41586-024-07045-4

Received: 11 June 2023

Accepted: 9 January 2024

Published online: 28 February 2024

Check for updates

Di Lu[1,8], Ruhong Li[1,8], Muhammad Mominur Rahman[2], Pengyun Yu[3,4], Ling Lv[1], Sheng Yang[5], Yiqiang Huang[1], Chuangchao Sun[1], Shuoqing Zhang[1], Haikuo Zhang[1], Junbo Zhang[1], Xuezhang Xiao[1], Tao Deng[6], Liwu Fan[5], Lixin Chen[1,7], Jianping Wang[3,4], Enyuan Hu[2]✉, Chunsheng Wang[6]✉ & Xiulin Fan[1]✉

Li-ion batteries (LIBs) for electric vehicles and aviation demand high energy density, fast charging and a wide operating temperature range, which are virtually impossible because they require electrolytes to simultaneously have high ionic conductivity, low solvation energy and low melting point and form an anion-derived inorganic interphase[1–5]. Here we report guidelines for designing such electrolytes by using small-sized solvents with low solvation energy. The tiny solvent in the secondary solvation sheath pulls out the Li^+ in the primary solvation sheath to form a fast ion-conduction ligand channel to enhance Li^+ transport, while the small-sized solvent with low solvation energy also allows the anion to enter the first Li^+ solvation shell to form an inorganic-rich interphase. The electrolyte-design concept is demonstrated by using fluoroacetonitrile (FAN) solvent. The electrolyte of 1.3 M lithium bis(fluorosulfonyl)imide (LiFSI) in FAN exhibits ultrahigh ionic conductivity of 40.3 mS cm^{-1} at 25 °C and 11.9 mS cm^{-1} even at −70 °C, thus enabling 4.5-V graphite||$LiNi_{0.8}Mn_{0.1}Co_{0.1}O_2$ pouch cells (1.2 Ah, 2.85 mAh cm^{-2}) to achieve high reversibility (0.62 Ah) when the cells are charged and discharged even at −65 °C. The electrolyte with small-sized solvents enables LIBs to simultaneously achieve high energy density, fast charging and a wide operating temperature range, which is unattainable for the current electrolyte design but is highly desired for extreme LIBs. This mechanism is generalizable and can be expanded to other metal-ion battery electrolytes.

Interactions between solvents, Li^+ cations and salt anions control the electrolyte properties, including ionic conductivity, solvation–desolvation behaviours and interphase chemistry[6,7]. The ethylene carbonate (EC)-based electrolytes with a strong interaction of Li^+-solvents have a high ionic conductivity (9–10 mS cm^{-1} at 25 °C) and form organic–inorganic solid electrolyte interphase (SEI) on graphite anodes, which enable graphite-based LIBs to achieve super-reversibility under mild working conditions[8]. However, the high desolvation energy and organic-rich SEI limit low-temperature performance owing to high interfacial resistance and freeze of EC-based electrolytes[9]. High-concentration electrolytes (HCEs), localized HCEs and weakly solvating electrolyte address the interfacial issues by forming anion-derived SEI (refs. 10–13), yet they invariantly have low ionic conductivities (around 1 mS cm^{-1}) owing to large viscosity and poor lithium-salt dissociation, which limits the charging rates and power densities[13,14]. It is impossible for the electrolyte to simultaneously have high ionic conductivity and form LiF-rich SEI, based on the current electrolyte-design principle.

Li^+ transport in liquid electrolytes with different salt concentrations can be through vehicular transport (Fig. 1a), structural transport (Fig. 1b) or a combination of both[15,16]. In basic carbonate liquid (dilute) electrolytes, vehicular transport is the dominant ionic conduction manner, in which Li^+ moves with its bulky solvation sheath[17,18]. However, in HCEs, Li^+ diffusion occurs mainly through hopping to solvents and anions by sequential shifts between various possible configurations of multidentate ligation through structural diffusion mechanism[19]. The high energy barrier in HCEs is primarily induced by stiff, percolated and interconnected ions with solvent/anion networks and close-knit coordination[20,21]. In both cases, only the Li^+ solvation energy in the first solvation sheath is considered because of the shielding effect from the large-sized solvents and anions in the primary solvation sheath. Therefore, weak bonding between Li^+ and solvents is desirable for allowing anions to enter the Li^+ primary solvation shell to form an anion-derived SEI. However, weak solvation substantially suppresses the full dissociation of lithium salts, resulting in a decrease in Li-ion conductivity. How to keep the benefit of weak bonding between Li^+ and anion/solvents while achieving a fast Li^+ transport in the liquid electrolyte remains an unsolved challenge for current organic-electrolyte design.

[1]State Key Laboratory of Silicon and Advanced Semiconductor Materials, School of Materials Science and Engineering, Zhejiang University, Hangzhou, China. [2]Chemistry Division, Brookhaven National Laboratory, Upton, NY, USA. [3]Beijing National Laboratory for Molecular Sciences, Molecular Reaction Dynamics Laboratory, CAS Research/Education Center for Excellence in Molecular Sciences, Institute of Chemistry, Chinese Academy of Sciences, Beijing, China. [4]University of the Chinese Academy of Sciences, Beijing, China. [5]State Key Laboratory of Clean Energy Utilization, School of Energy Engineering, Zhejiang University, Hangzhou, China. [6]Department of Chemical and Biomolecular Engineering, University of Maryland, College Park, MD, USA. [7]Key Laboratory of Advanced Materials and Applications for Batteries of Zhejiang Province, Hangzhou, China. [8]These authors contributed equally: Di Lu, Ruhong Li. ✉e-mail: enhu@bnl.gov; cswang@umd.edu; xlfan@zju.edu.cn

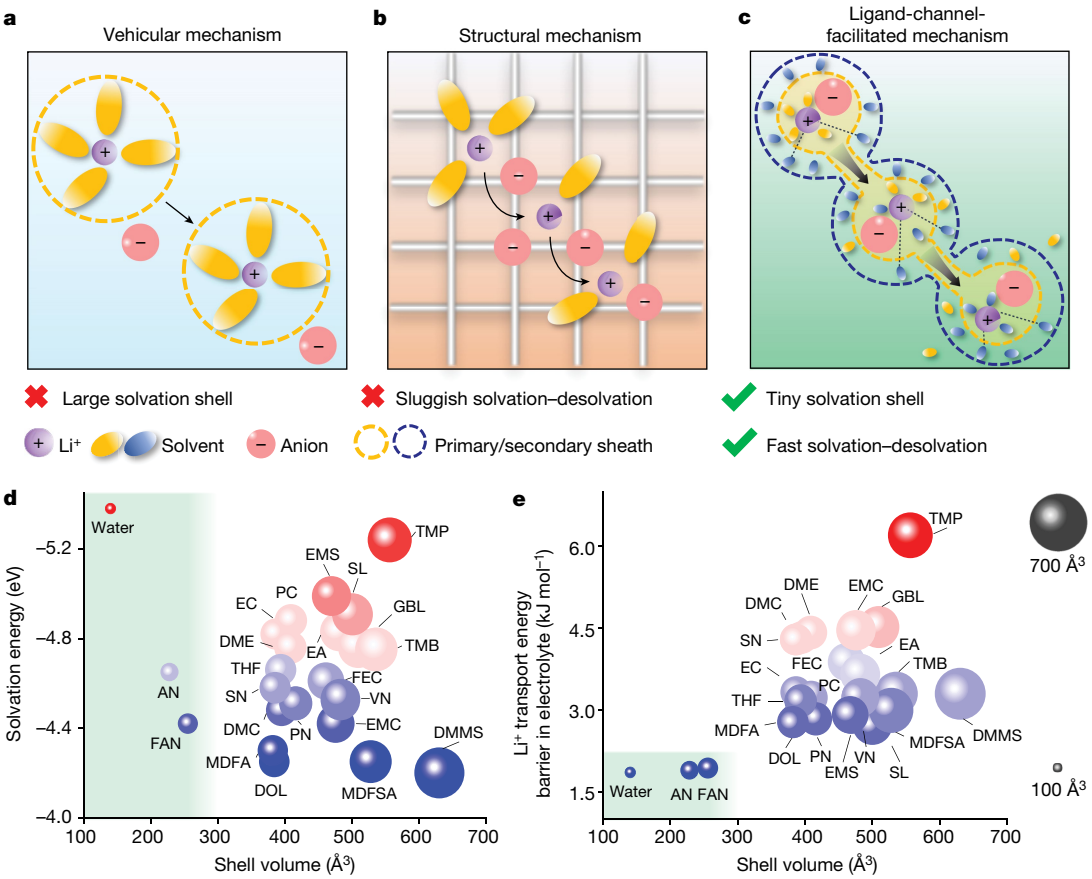

Fig. 1 | Electrolyte design and solvent-screening strategies. a–c, Schematic illustrations of Li^+ transport behaviours with the vehicular mechanism (**a**), structural mechanism (**b**) and ligand-channel-facilitated mechanism (**c**). **d**, The solvation energy and solvation-shell volume of solvents. **e**, The Li^+ transport energy barrier and solvation-shell volume of solvents. The electrolyte using the solvents with small size, low solvation energy and Li^+ transport energy barrier can conduct Li^+ through the ligand-channel transport mechanism. The full name of every solvent can be found in Supplementary Table 1.

Small-sized solvent with weak solvation energy and high Li-ion conductivity

Typically, a high degree of dissociation of lithium salt is positively correlated with high solvation energy[12,22]. The low solvation energy of the solvents enables the anion to enter the first solvation shell but reduces the ionic conductivity, whereas the high solvation energy of the solvents leads to high ionic conductivity but weakens the Li^+–anions interactions. We screened solvents based on the solvation energy (E_{sol}) in Fig. 1d. Among these solvents (Supplementary Table 1), 1,3-dioxolane (DOL), methyl difluoroacetate (MDFA), methyl 2,2-difluoro-2-(fluorosulfonyl) acetate (MDFSA) and dimethyldimethoxysilane (DMMS) show low solvation energy owing to the weak interaction with Li^+ (refs. 11,23,24), whereas trimethyl phosphate (TMP) and water (H_2O) exhibit the maximum solvation energy of −5.24 eV and −5.38 eV, respectively, owing to the strong coordination with Li^+ (refs. 25,26). Despite having similar solvation energy, acetonitrile (AN, −4.65 eV)/tetrahydrofuran (THF, −4.65 eV) and fluoroacetonitrile (FAN, −4.42 eV)/ethyl methyl carbonate (EMC, −4.42 eV) show notable disparity in lithium-salt dissociation (Supplementary Fig. 1a) and ionic conductivity (Supplementary Fig. 1b), suggesting that other parameters beyond solvation energy also play critical roles in determining the ionic conductivity of electrolyte. To gain a better understanding in this regard, we revisited the Li-ion transport mechanism in liquid electrolytes.

We calculated the Li-ion conductivity (σ) of electrolytes by incorporating both vehicular and structural transport mechanisms, involving key parameters such as solvation sheath volume (VN_s, in which V and N_s are the molecular volume of the solvent and the solvation number of Li^+, respectively; equations (1) and (2)) and Li^+ transport energy barrier (E_{trans}, free energy extracted from ab initio molecular dynamics (AIMD) trajectory of the probability distribution of Li^+-solvent among various Li^+ complexes; equation (3))[27,28] for fast Li-ion chemistries among a variety of solvents (Supplementary Table 1).

$$\sigma = \sum \frac{Z^2FC}{6\pi\eta r_s} \quad (1)$$

$$r_s^3 = \frac{3VN_s}{4\pi} + r_c^3 \quad (2)$$

$$\sigma = \frac{A}{T} C \exp\left(-\frac{E_{trans}}{k_B T}\right) \quad (3)$$

in which Z is the valence order; C is the molar concentration of diffused Li^+; F is Faraday's constant; η is the viscosity of electrolyte; r_s, and r_c are the Stokes radius of solvated Li^+ and the crystallographic radius of Li^+ (0.076 nm)[27], respectively; T is the absolute temperature; A and k_B are the pre-exponential factor and Boltzmann constant, respectively. According to the equations, the Li-ion conductivity increases as the Li^+ transport energy barrier (E_{trans}) and solvation sheaths volume (VN_s) decrease. On the basis of the above two parameters in Fig. 1e, three solvents, that is, H_2O (140.28 Å^3, 1.86 kJ mol^{-1}), AN (228.30 Å^3, 1.90 kJ mol^{-1}) and FAN (255.60 Å^3, 1.94 kJ mol^{-1}) with low Li^+ transport energy barrier and ultrasmall sheath volume stand out (light-green area), making them the most promising solvent candidates for the

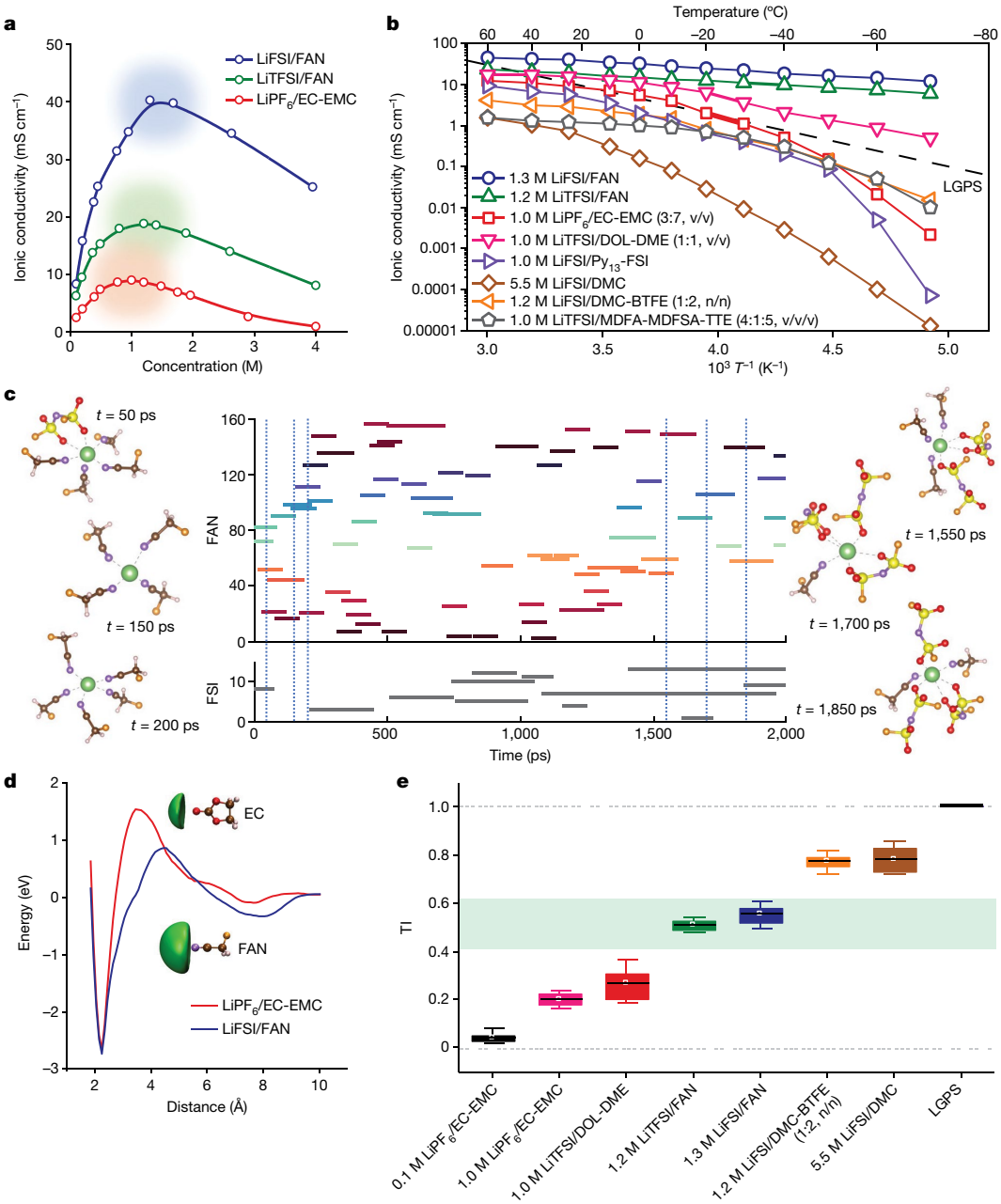

Fig. 2 | Physical properties and ion-transport mechanism of FAN-based electrolyte. a, Ionic conductivities of EC/EMC-based and FAN-based electrolytes with different concentrations. **b**, Ionic conductivities of liquid and solid-state electrolytes from 60 °C to −70 °C. **c**, Evolution of Li-ion solvation environment in 1.3 M LiFSI/FAN electrolyte from molecular dynamics simulations at 298 K (the vertical axis represents the serial number of different solvents or anions coordinated with the investigated Li^+ in the simulation time of 2,000 ps). The short horizontal lines denote the residence time of N(FAN) within 3.0 Å and O(FSI^-) within 3.0 Å of Li^+. The representative Li^+ solvation structures corresponding to different residence times indicated by dashed vertical lines are also shown (t = 50 ps, 150 ps, 200 ps, 1,550 ps, 1,700 ps, 1,850 ps; green, Li atom; red, O atom; yellow, S atom; purple, N atom; orange, F atom; tan, C atom; white, H atom). **d**, Variation of energy barrier of Li^+ hopping in different electrolytes. Insets, spatial distribution function of Li^+ ions around FAN and EC solvents. **e**, TI of different electrolytes. The error bars represent maximum and minimum values of the TI. The mean values of the TI are marked with black lines.

electrolyte with ultrahigh ionic conductivity. Owing to the limited screening effect, these three small-sized solvents in the secondary solvation sheath can interact with inner Li^+ and regulate solvated structures (Supplementary Fig. 2) to form continuous Li^+ transporting 'ligands' channels (Fig. 1c), thus facilitating fast ion chemistries. Excluding H_2O and AN as solvents because of their high reactivity and poor SEI-formation capability to the anodes (Supplementary Fig. 3 and Supplementary Note 1), only FAN satisfies the electrolyte-design criteria of low solvation energy, low Li^+ transport energy barrier and small solvent size, thereby facilitating the formation of LiF-rich SEI and promising high ionic conductivity through a fast ion-conduction ligand channel.

To validate the electrolyte-design criteria, we prepared 1.3 M LiFSI/FAN electrolyte, which achieves an ultrahigh ionic conductivity of 40.3 mS cm^{-1} at 25 °C in Fig. 2a. This value is more than four times higher than that of typical carbonate-based electrolytes, such as 1.0 M lithium hexafluorophosphate ($LiPF_6$)/EC-EMC (3:7, v/v) electrolyte (9.0 mS cm^{-1}). The high ionic conductivity of FAN-based electrolyte

holds when other salts such as lithium bis(trifluoromethanesulfonyl) imide (LiTFSI) or $LiPF_6$ are used (Fig. 2a and Supplementary Table 2). Figure 2b and Supplementary Figs. 4 and 5 summarize the ionic conductivities of FAN-based electrolytes and seven typical electrolytes between 60 °C and −70 °C (Supplementary Note 2). It shows that the ionic conductivity of conventional carbonate-based electrolyte exhibits an inflection point at −20 °C, with a low value of 2.0 mS cm^{-1}, which is followed by a rapid decline owing to solidification of the electrolyte. By contrast, LiFSI/FAN electrolyte achieves the highest ionic conductivity of 11.9 mS cm^{-1} even at −70 °C, which is more than four orders of magnitude greater than that of traditional carbonate-based electrolyte and surpasses the ionic conductivities of the state-of-the-art electrolytes, including liquefied gas electrolyte (5.8 mS cm^{-1}, −60 °C)[29], ethyl-acetate-based electrolyte (0.2 mS cm^{-1}, −70 °C)[30] and fluorinated-acetate-based electrolyte (0.01 mS cm^{-1}, −70 °C)[24]. Notably, the characteristic curves (log σ versus $1/T$) of 1.3 M LiFSI/FAN and 1.2 M LiTFSI/FAN are straight and parallel to each other (Fig. 2b), indicating ultralow glass-transition temperature of FAN-based electrolytes (Supplementary Figs. 6–9 and Supplementary Note 3). As well as ionic conductivity, other transport parameters, that is, transference number and self-diffusion coefficient, also highlight the fast ion-conduction capability of FAN-based electrolytes (Supplementary Table 3).

Ligand-channel-facilitated mechanism

To understand the ligand-channel-facilitated mechanism, we performed molecular dynamics simulations to investigate the molecular-scale solvation dynamics and the anion/solvent residence times around the Li^+ cations, as shown in Fig. 2c and Supplementary Fig. 10. Our results show that the residence time of Li^+ in 1.3 M LiFSI/FAN electrolyte with the ligand-channel-facilitated mechanism is exceptionally short, suggesting that Li^+ is frequently solvated by FAN molecules (about 77.2 ps at 298 K) and FSI^- anions (about 136.8 ps at 298 K) with ultrafast hopping frequencies. Such short residence time always results in a high Li^+ hopping frequency between the neighbouring coordination sites and, thereby, high ionic conductivity[31]. This energetic Li^+ hopping is also verified by the decreased activation energy (0.85 eV; Fig. 2d) and the large spatial distribution of Li^+ ions around FAN solvent, as well as the long attracting distance of Li^+-FAN clusters (Fig. 2d inset and Supplementary Fig. 2). In conventional carbonate electrolytes, Li^+ diffusion occurs by means of the vehicular mechanism, in which Li^+ is carried along by the EC/EMC solvation sheaths with a longer coordination period (about 198.5 ps at 298 K), owing to the strong affinity of solvated Li^+-inner EC/EMC molecules[31,32] (Supplementary Fig. 10a). With the increase of salt concentration, the Li^+ transport mechanism gradually transforms into a structural one, in which Li^+ predominantly exchanges with FSI^- anions (about 885.3 ps at 298 K; Supplementary Fig. 10b). Furthermore, the femtosecond two-dimensional infrared spectroscopy also provides solid structural evidence for the ligand-channel-facilitated mechanism for FAN-based electrolyte (Supplementary Figs. 11–13, Supplementary Table 4 and Supplementary Note 4).

The maximum ionic conductivity can be achieved during the transition from vehicular transport to structural transport. To gain insight into the fast Li^+ conduction mechanism in an electrolyte, we introduced the transport index (TI) as a new parameter to quantify Li^+ transport behaviour, which represents the percentage of structural Li-ion transport in total Li-ion transport (equation (4); the details are shown in Supplementary Fig. 14 and Supplementary Note 5). In equation (4), N is the number of transport ions (Li^+), t_V is the time for Li^+ transport without solvent/anion exchange and t_S is the time for Li^+ transport accompanied by solvent/anion hopping. It is worth noting that the sum of t_V and t_S equals the total simulation time. $\Delta r_{i,j}$ and $\Delta r_{i,k}$ are the displacements of Li^+ that obey different types of ion-motion mechanism in a given time interval.

$$\mathrm{TI} = \frac{S}{V+S} = \frac{1}{N}\sum_{i=1}^{N}\left(\frac{\sum_{k=0}^{t_S}\Delta r_{i,k}{}^2}{\sum_{j=0}^{t_V}\Delta r_{i,j}{}^2+\sum_{k=0}^{t_S}\Delta r_{i,k}{}^2}\right) \quad (4)$$

At TI = 0 (ideal dilute liquid electrolytes), the ion transport occurs by the vehicular mechanism. At TI = 1 (solid-state electrolyte), the Li^+ percolation with structural mechanism contributes to the integral Li^+ motion (Supplementary Fig. 15). By clarifying the two parameters of ionic conductivity and TI in liquid electrolytes, the ion-transport mode can be revealed at the molecular level. For the standout electrolytes with the ligand-channel-facilitated mechanism, the maximum ionic conductivity is achieved when the TI is around 0.5 (Supplementary Fig. 16) and vice versa, which suggests a unique and ultrafast ion-transport behaviour that is different from vehicular/structural ones. As shown in Fig. 2a,e and Supplementary Fig. 14, FAN-based electrolyte with a concentration of 1.3 M and a TI value of approximately 0.5 presents the fastest ion-translation property, far exceeding any other electrolytes. It is noteworthy that the TI can be considered as a direct and efficient parameter to design ideal electrolytes with superionic behaviour.

Electrochemical performances at extreme conditions

Similar to the classical case of 'EC–PC disparity'[33], the minuscule structural difference between AN and FAN caused by a single F atom leads to two totally distinct interphase behaviours: the continuously irreversible reduction of AN-based electrolyte at about 0.5 V, as opposed to the reversible Li^+ interaction/deintercalation enabled by FAN-based electrolyte at about 0.1 V (Supplementary Figs. 17 and 18 and Supplementary Note 6). Furthermore, the optimized solvation structures (Supplementary Figs. 19–21 and Supplementary Note 7) of FAN and AN-based electrolytes after single-electron reduction are shown in Supplementary Fig. 22. The reductive decomposition of both FAN and FSI^- generate a large amount of LiF species, which favour the interphase chemistries.

To eliminate the adverse effect of Li metal polarization on the electrochemical performance, the rate performances of graphite electrodes with different electrolytes were tested using three-electrode Li||graphite cells[34] (Supplementary Fig. 23). Owing to the small impedances and overpotentials of the cells with FAN-based electrolyte at all rates (Supplementary Figs. 24 and 25 and Supplementary Table 5), the cells with FAN-based electrolyte exhibit superior rate capability (Supplementary Note 8). Notably, the FAN-based electrolyte enables graphite||NMC811 full cells to operate effectively under extreme conditions (high voltage, high rate and wide temperature range) without Al current collector corrosion (Supplementary Fig. 26). In Fig. 3a,b, a graphite||NMC811 full cell with FAN-based electrolyte yields a capacity of 177.8 mAh g^{-1} at 6C (76.4 mAh g^{-1} for EC/EMC-based electrolyte) and shows unprecedented capacity retention of 80% over 3,000 cycles at 6C with an average Coulombic efficiency of 99.97%, which represents the lowest capacity loss reported so far for graphite||NMC811 cells at such a high charge–discharge rate. Although nitriles have been widely used as an effective additive for high-voltage cathodes[35,36], FAN, as the fluorinated nitrile, exhibits even better anodic stability (Supplementary Fig. 27). The 4.5-V graphite||NMC811 cell with high loading of 2 mAh cm^{-2} delivers a highly reversible capacity of 173.9 mAh g^{-1} at 4C in FAN-based electrolyte, whereas that of EC/EMC-based electrolyte only remains at 28.3 mAh g^{-1} (Supplementary Fig. 28).

Benefitting from the unique ligand-channel-facilitated transport mechanism with TI ≈ 0.5 in the wide temperature range (Supplementary Figs. 29–31 and Supplementary Note 9), FAN-based electrolyte supports high reversibility of graphite||NMC811 full cells in a wide temperature window ranging from −80 °C to +60 °C (Fig. 3c,d). The graphite||NMC811 full cells with FAN-based electrolyte show a high capacity of 175.0 mAh g^{-1} at 6C and stable cycling performance

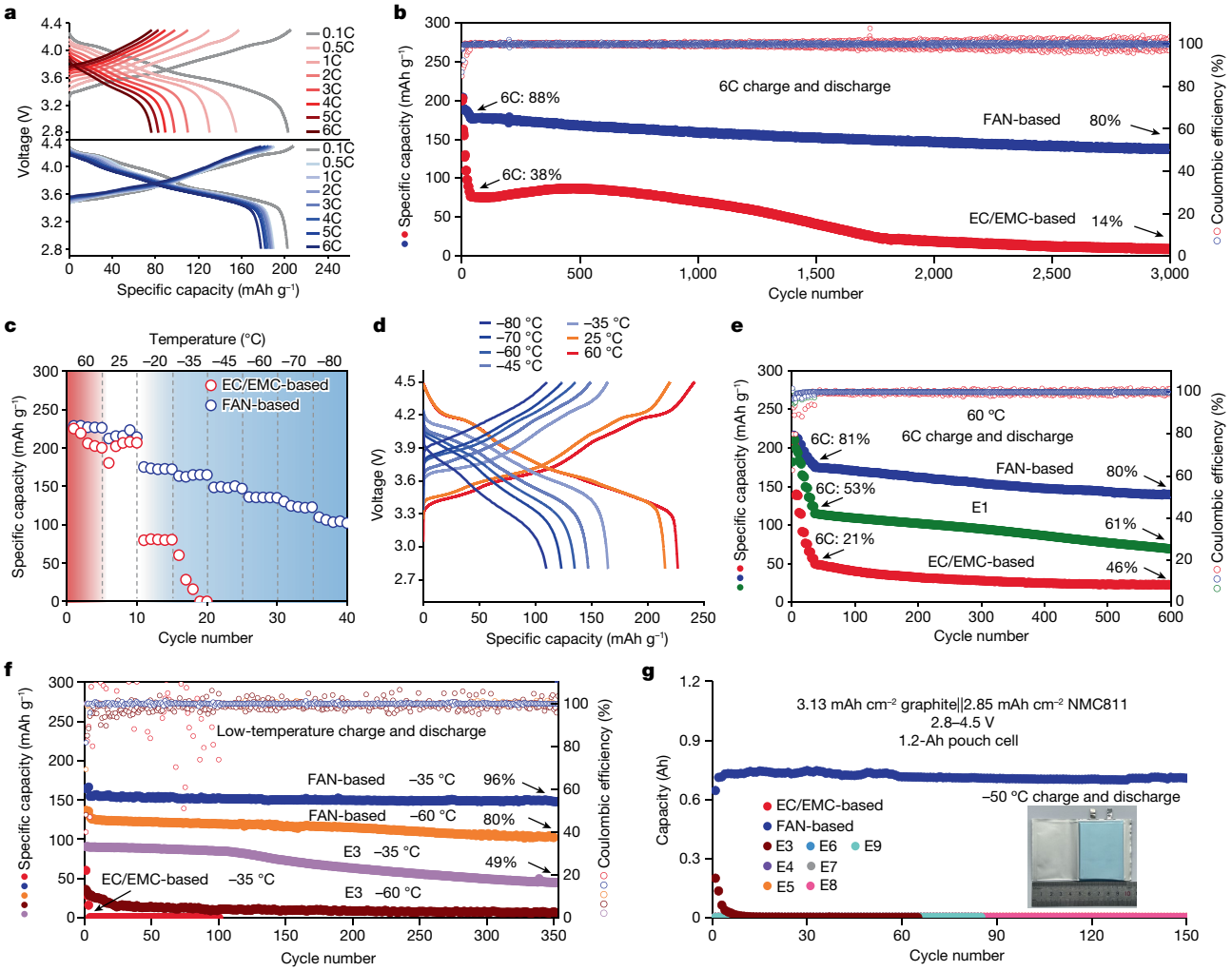

Fig. 3 | Electrochemical performances of FAN-based electrolyte at extreme conditions. a, Charge–discharge curves of graphite||NMC811 cells at different rates for EC/EMC-based (top) and FAN-based electrolyte (bottom) at 25 °C. **b**, Cycling performance of graphite||NMC811 cells with different electrolytes in the range 2.8–4.3 V at 25 °C (0.1C, 0.5C, 1C, 2C, 3C, 4C, 5C and 6C, each cycled for five cycles and then 6C for long cycling). Specific capacities (**c**) and charge–discharge curves (**d**) of graphite||NMC811 cells with FAN-based electrolyte in the range 2.8–4.5 V at different temperatures. **e**, Cycling performance of graphite||NMC811 cells with different electrolytes in the range 2.8–4.3 V at 60 °C (0.1C, 0.5C, 1C, 2C, 3C, 4C, 5C and 6C, each cycled for five cycles and then 6C for long cycling). **f**, Cycling performance of graphite||NMC811 cells with different electrolytes in the range 2.8–4.5 V at −35 °C and −60 °C. **g**, Cycling performance of graphite||NMC811 pouch cells with different electrolytes in the range 2.8–4.5 V at −50 °C. The electrolytes E1–E9 are listed in Supplementary Table 6.

with a capacity retention of 80% after 600 cycles with an average Coulombic efficiency of 99.95% at 60 °C (Fig. 3e and Supplementary Fig. 32). It is worth noting that low-temperature charging is particularly challenging for graphite-based LIBs, therefore previous studies mainly focused on low-temperature discharging[12,24,37]. In the current work, the FAN-based electrolyte exhibits excellent performance for both charging and discharging at ultralow temperatures. The graphite||NMC811 full cells using this electrolyte demonstrate high retention of their room-temperature capacity, with 76% (164.8 mAh g^{-1}), 63% (135.0 mAh g^{-1}) and 51% (109.7 mAh g^{-1}) retention at −35 °C, −60 °C and −80 °C, respectively. Moreover, the graphite||NMC811 cells with FAN-based electrolyte show extremely stable and reversible capacity over 350 cycles at −35 °C (capacity retention of 96%, average Coulombic efficiency of 99.95%) and −60 °C (capacity retention of 80%, average Coulombic efficiency of 99.93%) without Li plating (Fig. 3f and Supplementary Fig. 33), whereas the cells using EC/EMC-based electrolyte cannot provide any capacity (Supplementary Fig. 34). Also, we compared the electrochemical performance of reported electrolytes (E1–E9; details in Supplementary Table 6) at extreme temperatures (Supplementary Figs. 35–37 and Supplementary Note 10). In a scaled-up cell format, 1.2-Ah graphite||NMC811 pouch cells (area capacity of cathode/anode: 2.85 mAh cm^{-2}/3.13 mAh cm^{-2}) with lean electrolyte (3 g Ah^{-1}) were further evaluated in Fig. 3g. Notably, the 1.2-Ah pouch cell with FAN-based electrolyte can deliver a reversible capacity of about 0.73 Ah, which was charged and discharged at −50 °C, maintaining high reversibility without any capacity decay over 150 cycles, whereas that with E3–E9 electrolytes (details in Supplementary Table 6) cannot show any capacity. When the temperature drops to −65 °C, −70 °C and −80 °C, the 1.2-Ah graphite||NMC811 pouch cells with FAN-based electrolyte still exhibit reversible capacities of 0.62 Ah, 0.55 Ah and 0.45 Ah, respectively (Supplementary Fig. 38). These findings indicate a marked advancement in the rechargeability of graphite anodes under ultralow temperatures and ultrahigh rates, thus validating the electrolyte-design principles for fast Li-ion chemistries.

Chemistry at the interphase

The SEI formed on graphite anode in 1.3 M LiFSI/FAN electrolyte is designed to be rich in LiF–Li_xN, as confirmed by high-resolution

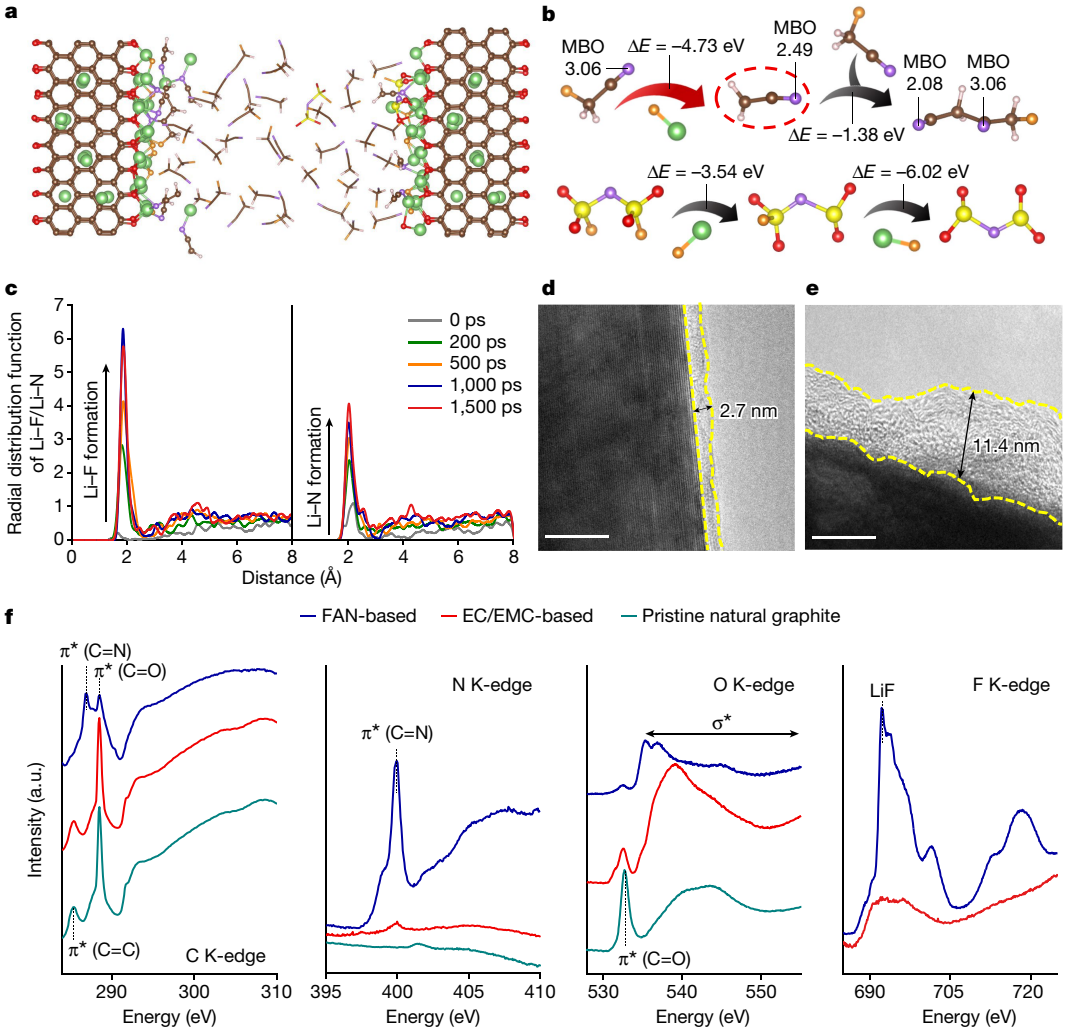

Fig. 4 | FAN-based electrolyte/electrode interphase analysis. a, The initial decomposition reaction of FAN-based electrolyte on the anode interphase calculated by AIMD. **b**, Energetics for multistep decomposition pathways of FAN solvent and FSI^- anion and MBO of C=N bonds (the dashed red ellipse represents the most decomposed product). **c**, Radial distribution function curves of Li–F (left) and Li–N (right). **d**,**e**, High-resolution transmission electron microscopy images of graphite anodes recovered from graphite||NMC811 cells using FAN-based (**d**) and EC/EMC-based (**e**) electrolyte after 100 cycles, respectively. Scale bars, 10 nm. **f**, Characterization of pristine and cycled graphite anodes (after 100 cycles) by the total electron yield mode of soft XAS: C K-edge, N K-edge, O K-edge and F K-edge. The probing depth of soft XAS in the total electron yield mode is around 10 nm. a.u., arbitrary units.

transmission electron microscopy, soft X-ray absolution spectroscopy (XAS) and theoretical calculations. During the initial decomposition reactions of FAN-based electrolyte in Fig. 4a–c, the FSI^- anions form anion-derived SEI by gradually accepting electrons. Simultaneously, FAN solvents are prone to being reduced with the lowest reaction energy of −4.73 eV, resulting in the formation of LiF–Li_xN-rich SEI. The value of Mayer bond order (MBO) of C≡N is reduced from 3.06 to 2.49 and 2.08, suggesting that substantial C=N moieties are generated over cycling. These findings are consistent with the in-depth X-ray photoelectron spectroscopy (XPS) results (Supplementary Figs. 39–41). By contrast, EC/EMC-based electrolyte tends to produce considerable organic Li–O species on graphite anode during the initial decomposition reactions (Supplementary Figs. 42 and 43), which leads to sluggish Li^+ transport kinetics. As shown in Fig. 4d,e, the SEI formed by the FAN-based electrolyte is more uniform and thinner (2.7 nm) compared with the SEI formed by EC/EMC-based electrolyte (11.4 nm). Such homogenous interphase films are also detected on NMC811 cycled in FAN-based electrolyte (Supplementary Fig. 44). In Fig. 4f, the appearance of new species of C=N (286.8 eV, C K-edge and 399.8 eV, N K-edge) and LiF (692.2 eV, F K-edge) on graphite anode cycled in FAN-based electrolyte indicates the decomposition of FAN solvent, which is consistent with AIMD results (Fig. 4a–c and Supplementary Fig. 43). Meanwhile, the C=N and LiF species are also observed in the bulk structures of graphite anode (FY mode of XAS, as shown in Supplementary Fig. 45), suggesting that the initial decomposition of FSI^- anions and FAN solvents, followed by further decomposition of FAN solvent, helps to improve the stability of bulk graphite anode. This effective and low-resistance SEI-formation mechanism promotes the achievement of ultrafast LIBs under extreme conditions.

Conclusion

In summary, the ideal electrolyte requires contradictory properties of high salt dissociation but low Li^+ transport energy barrier and high ionic conductivity but inorganic-rich interphase, which are never achieved simultaneously. Taking advantage of the ligand-channel-facilitated mechanism, we designed a unique electrolyte (1.3 M LiFSI/FAN) with small solvation sheath and fast solvation–desolvation capability. The FAN-based electrolyte demonstrates an ultrahigh ionic conductivity of 40.3 mS cm^{-1} at 25 °C and 11.9 mS cm^{-1} at −70 °C. It also realizes fast charge-transfer kinetics and promotes the formation of conductive LiF–Li_xN-rich SEI, which overcomes the sluggish kinetics of graphite during ultrafast charging and ultralow temperature conditions.

The graphite||NMC811 full cell with FAN-based electrolyte exhibits >3,000 cycles life at 6C and delivers a high reversible capacity of 109.7 mAh g^{-1} when charged and discharged at −80 °C. Practical 1.2-Ah graphite||NMC811 pouch cells using FAN-based electrolyte deliver highly reversible capacity of 0.73 Ah at −50 °C (0.62 Ah at −65 °C), with no capacity decay after 150 cycles. This work sheds light on ion motion between the vehicular and structural mechanisms. The ligand-channel-facilitated conduction mechanism paves the way for high-energy batteries operating at extreme conditions.

Online content

Any methods, additional references, Nature Portfolio reporting summaries, source data, extended data, supplementary information, acknowledgements, peer review information; details of author contributions and competing interests; and statements of data and code availability are available at https://doi.org/10.1038/s41586-024-07045-4.

1. Tarascon, J.-M. & Armand, M. Issues and challenges facing rechargeable lithium batteries. *Nature* **414**, 359–367 (2001).
2. Dunn, B., Kamath, H. & Tarascon, J.-M. Electrical energy storage for the grid: a battery of choices. *Science* **334**, 928–935 (2011).
3. Rodrigues, M.-T. F. et al. A materials perspective on Li-ion batteries at extreme temperatures. *Nat. Energy* **2**, 17108 (2017).
4. Liu, Y., Zhu, Y. & Cui, Y. Challenges and opportunities towards fast-charging battery materials. *Nat. Energy* **4**, 540–550 (2019).
5. Fan, X. & Wang, C. High-voltage liquid electrolytes for Li batteries: progress and perspectives. *Chem. Soc. Rev.* **50**, 10486–10566 (2021).
6. Xu, K. Nonaqueous liquid electrolytes for lithium-based rechargeable batteries. *Chem. Rev.* **104**, 4303–4417 (2004).
7. Yao, N., Chen, X., Fu, Z.-H. & Zhang, Q. Applying classical, *ab initio*, and machine-learning molecular dynamics simulations to the liquid electrolyte for rechargeable batteries. *Chem. Rev.* **122**, 10970–11021 (2022).
8. Gupta, A. & Manthiram, A. Designing advanced lithium-based batteries for low-temperature conditions. *Adv. Energy Mater.* **10**, 2001972 (2020).
9. Zhang, S., Xu, K. & Jow, T. The low temperature performance of Li-ion batteries. *J. Power Sources* **115**, 137–140 (2003).
10. Yu, Z. et al. Molecular design for electrolyte solvents enabling energy-dense and long-cycling lithium metal batteries. *Nat. Energy* **5**, 526–533 (2020).
11. Huang, Y. et al. Eco-friendly electrolytes via a robust bond design for high-energy Li metal batteries. *Energy Environ. Sci.* **15**, 4349–4361 (2022).
12. Fan, X. et al. All-temperature batteries enabled by fluorinated electrolytes with non-polar solvents. *Nat. Energy* **4**, 882–890 (2019).
13. Yao, Y. et al. Regulating interfacial chemistry in lithium-ion batteries by a weakly solvating electrolyte. *Angew. Chem. Int. Ed.* **60**, 4090–4097 (2021).
14. Jiang, L. et al. Inhibiting solvent co-intercalation in a graphite anode by a localized high-concentration electrolyte in fast-charging batteries. *Angew. Chem. Int. Ed.* **60**, 3402–3406 (2021).
15. Self, J., Fong, K. D. & Persson, K. A. Transport in superconcentrated $LiPF_6$ and $LiBF_4$/propylene carbonate electrolytes. *ACS Energy Lett.* **4**, 2843–2849 (2019).
16. Siegel, D. J., Nazar, L., Chiang, Y.-M., Fang, C. & Balsara, N. P. Establishing a unified framework for ion solvation and transport in liquid and solid electrolytes. *Trends Chem.* **3**, 807–818 (2021).
17. Aihara, Y., Sugimoto, K., Price, W. S. & Hayamizu, K. Ionic conduction and self-diffusion near infinitesimal concentration in lithium salt-organic solvent electrolytes. *J. Chem. Phys.* **113**, 1981–1991 (2000).
18. Borodin, O. & Smith, G. D. Li^+ transport mechanism in oligo(ethylene oxide)s compared to carbonates. *J. Solut. Chem.* **36**, 803–813 (2007).
19. Yamada, Y., Wang, J., Ko, S., Watanabe, E. & Yamada, A. Advances and issues in developing salt-concentrated battery electrolytes. *Nat. Energy* **4**, 269–280 (2019).
20. Borodin, O. et al. Liquid structure with nano-heterogeneity promotes cationic transport in concentrated electrolytes. *ACS Nano* **11**, 10462–10471 (2017).
21. Okoshi, M., Chou, C. P. & Nakai, H. Theoretical analysis of carrier ion diffusion in superconcentrated electrolyte solutions for sodium-ion batteries. *J. Phys. Chem. B* **122**, 2600–2609 (2018).
22. Borodin, O., Self, J., Persson, K. A., Wang, C. & Xu, K. Uncharted waters: super-concentrated electrolytes. *Joule* **4**, 69–100 (2020).
23. Sun, C. et al. 50C fast-charge Li-ion batteries using a graphite anode. *Adv. Mater.* **34**, 2206020 (2022).
24. Xu, J. et al. Electrolyte design for Li-ion batteries under extreme operating conditions. *Nature* **614**, 694–700 (2023).
25. Ren, X. et al. Role of inner solvation sheath within salt–solvent complexes in tailoring electrode/electrolyte interphases for lithium metal batteries. *Proc. Natl Acad. Sci.* **117**, 28603–28613 (2020).
26. Suo, L. et al. "Water-in-salt" electrolyte enables high-voltage aqueous lithium-ion chemistries. *Science* **350**, 938–943 (2015).
27. Ue, M. & Mori, S. Mobility and ionic association of lithium salts in a propylene carbonate-ethyl methyl carbonate mixed solvent. *J. Electrochem. Soc.* **142**, 2577–2581 (1995).
28. Ren, Y. et al. Oxide electrolytes for lithium batteries. *J. Am. Ceram. Soc.* **98**, 3603–3623 (2015).
29. Yang, Y. et al. Liquefied gas electrolytes for wide-temperature lithium metal batteries. *Energy Environ. Sci.* **13**, 2209–2219 (2020).
30. Dong, X., Guo, Z., Guo, Z., Wang, Y. & Xia, Y. Organic batteries operated at −70°C. *Joule* **2**, 902–913 (2018).
31. Seo, D. M. et al. Electrolyte solvation and ionic association III. Acetonitrile-lithium salt mixtures–transport properties. *J. Electrochem. Soc.* **160**, A1061–A1070 (2013).
32. Kreuer, K.-D., Rabenau, A. & Weppner, W. Vehicle mechanism, a new model for the interpretation of the conductivity of fast proton conductors. *Angew. Chem. Int. Ed. Engl.* **21**, 208–209 (1982).
33. Xing, L. et al. Deciphering the ethylene carbonate–propylene carbonate mystery in Li-ion batteries. *Acc. Chem. Res.* **51**, 282–289 (2018).
34. Yao, Y.-X. et al. Unlocking charge transfer limitations for extreme fast charging of Li-ion batteries. *Angew. Chem. Int. Ed.* **62**, e202214828 (2023).
35. Yang, X. et al. Enabling stable high-voltage $LiCoO_2$ operation by using synergetic interfacial modification strategy. *Adv. Funct. Mater.* **30**, 2004664 (2020).
36. Zhi, H., Xing, L., Zheng, X., Xu, K. & Li, W. Understanding how nitriles stabilize electrolyte/electrode interface at high voltage. *J. Phys. Chem. Lett.* **8**, 6048–6052 (2017).
37. Gao, Y. et al. Low-temperature and high-rate-charging lithium metal batteries enabled by an electrochemically active monolayer-regulated interface. *Nat. Energy* **5**, 534–542 (2020).

Methods

Preparation of electrolytes and electrodes

Battery-grade $LiPF_6$, LiFSI, LiTFSI and Py_{13}-FSI were purchased from Changde Dadu New Material Co., Ltd. EC, EMC, DMC, DME, DOL, BTFE, AN and FAN were purchased from Sigma-Aldrich. The EC/EMC-based electrolyte and FAN-based electrolyte were 1.0 M $LiPF_6$/EC-EMC (3:7, v/v) and 1.3 M LiFSI/FAN, respectively. All solvents were dried over activated molecular sieves before use. All electrolytes were prepared in an argon-filled glovebox (Mikrouna, China) with moisture and oxygen contents less than 0.1 ppm. The solid-state electrolyte $Li_{10}GeP_2S_{12}$ (LGPS) was synthesized according to previously reported procedures[38,39].

The anode slurry coated on copper foil was composed of 80 wt% natural graphite (graphite, average diameters: 2.5 μm, Beijing Xinjincheng Science and Trade Co., Ltd.), 10 wt% conductive carbon black (Super C45, Hefei Kejing Materials Technology Co., Ltd.), 10 wt% PAALi (Sigma-Aldrich) and pure H_2O as solvent. The cathode slurry coated on aluminium foil consisted of 80 wt% NMC811 (Hefei Kejing Materials Technology Co., Ltd.), 10 wt% conductive carbon black (Super C45, Hefei Kejing Materials Technology Co., Ltd.), 10 wt% polyvinylidene fluoride binder (PVDF, Suzhou Zhongyan Chemical Technology Co., Ltd.) and N-methyl-2-pyrrolidinone (NMP, Suzhou Zhongyan Chemical Technology Co., Ltd.) as solvent. After solvents have been dried, the electrodes were punched into discs with diameters of 14 mm and 12 mm for anodes and cathodes, respectively, followed by further vacuum drying at 100 °C overnight before the assembling of both half cells and full cells. The mass loading of NMC811 and graphite for coin cells were about 5.00 mg cm^{-2} and 2.95 mg cm^{-2}, respectively. Coin cells with as-prepared electrolytes (80 μl) were assembled with NMC811 (or graphite) as working electrode and polyethylene membrane (ND16, SK Innovation Co., Ltd.) as separator. For coin full cells, the N/P value was 1.1 (calculated according to 200 mAh g^{-1} for NMC811 and 372 mAh g^{-1} for graphite). The graphite||NMC811 pouch-type cells (1.2 Ah) (Li-FUN Technology Co., Ltd.) were injected with 3 g Ah^{-1} electrolytes before sealing. Owing to incompatibility between Li metal and AN solvent, co-intercalate behaviour of AN-based electrolyte was investigated by graphite||4 mAh cm^{-2} $LiFePO_4$ full cell. The viscosity of electrolytes was measured by an Anton Paar MCR102e Rheometer. Different electrolytes subjected to differential scanning calorimetry measurement were packed in a stainless-steel pan, which was then crimp-sealed in a glovebox filled with argon. All of the differential scanning calorimetry experiments were carried out at a cooling/heating rate of 5 °C min^{-1}.

Electrochemical measurements

All cells were both charged and discharged at the same temperature between −80 °C to 60 °C instead of previously reported room-temperature charging and low-temperature discharging protocol using a LAND battery testing system (Wuhan LAND Electronics Co., Ltd.). For coin-type cells at extreme conditions, the graphite||NMC811 cells were cycled at 0.5C for the first ten cycles at room temperature, followed by long cycling at 0.2C at low temperatures (−35 to −60 °C, 0.1C for −70 and −80 °C). For pouch-type cells at extreme conditions, the graphite||NMC811 cells were cycled at 0.2C for the first ten cycles at room temperature, followed by long cycling at 0.1C at low temperatures (−50 °C and −65 °C). In galvanostatic intermittent titration technique measurements, the Li||graphite cells were cycled at a rate of 10C and 3 h rest time (after 60 cycles at 10C charge and discharge). Two plate electrodes were inserted into electrolytes (6 ml) to measure the ionic conductivities of the electrolytes by an AC impedance analysis using an Ivium-n-Stat with an AC voltage amplitude of 10 mV over the frequency range from 1 Hz to 1 MHz at various temperatures and concentrations. The electrochemical impedance spectroscopy spectra of coin cells at fully discharged state were performed by an electrochemical workstation (Ivium-n-Stat, Ivium Technologies BV Co., Ltd.) over frequencies from 10 kHz to 10 mHz with a voltage amplitude of 10 mV.

Characterization

The solvation structures of different electrolytes were measured by ^{7}Li and ^{19}F nuclear magnetic resonance spectroscopy (600 MHz NMR Spectrometer, Agilent DD2 600). The cathodes and anodes were disassembled from graphite||NMC811 full cells cycled 100 cycles and rinsed with anhydrous DMC three times to remove the residuals (inside the glovebox), followed by characterizations of scanning electron microscopy (SU-70, Hitachi Ltd.), transmission electron microscopy (Tecnai G2 F20) and XPS (ESCALAB 250Xi, Thermo Fisher Scientific). Samples were transferred directly to the XPS sample chamber to avoid interference from the external rings. XAS of anodes were performed at beamline 23-ID-2 of the National Synchrotron Light Source II (NSLS II) at Brookhaven National Laboratory. The soft XAS measurements for obtaining interspatial and bulk information were conducted in both total electron yield and fluorescence yield modes at the IOS beamline of NSLS II. The collected XAS data were analysed using the ATHENA software package.

Quantum chemistry calculations

All quantum chemistry calculations were performed using Gaussian 16 software. The M06-2X functional was used as it was shown to accurately describe long-range van der Waals interaction of intermolecular interactions. The triple-zeta basis set def2-TZVP was used for structure optimization as well as the energy calculation. All of the optimized structures were confirmed as potential minima, with no frequency modes with imaginary eigenvalues, through frequency analyses following geometry optimizations. The SMD implicit solvation model with AN (ε = 35.688) was used to represent different electrolyte environments not explicitly included in quantum chemistry calculations.

The solvation energy of the nth solvent (AN and FAN) is defined as the energy difference between (LiFSI: n solvent) and (LiFSI: (n − 1) solvent) and solvent. The solvation energy of FSI^- with the (Li^+: n solvent) is defined as the energy difference between (LiFSI: n solvent) and (Li^+: n solvent) and FSI^-. The MBO was calculated by using the Multiwfn 3.8 program.

Classical molecular dynamics simulations

Classical molecular dynamics simulations were performed in LAMMPS using the all-atom optimized potentials for liquid simulations (OPLS-AA) force field with the Li^+, PF_6^- and FSI^- anions description from previous publications. The electrolyte systems were set up initially with the salt and solvent molecules distributed in the simulation boxes using Moltemplate (http://www.moltemplate.org/). For each system, an initial energy minimization at 0 K (energy and force tolerances of 10^{-5}) was performed to obtain the ground-state structure. After this, the system was slowly heated from 0 K to room temperature (298 K) at a constant volume over 0.2 ns using a Langevin thermostat, with a damping parameter of 100 ps. The system was equilibrated at constant temperature (298 K) and constant pressure (1 bar) (NPT ensemble) for 5 ns. For production runs, a series of 10-ns simulations at 300 K were carried out in the NVT ensemble using a Nosé–Hoover thermostat with a coupling constant of 0.1 ps. Radial distribution functions were obtained using the Visual Molecular Dynamics software. Snapshots of the most probable solvation sheaths were also sampled from the simulation trajectory using VESTA.

The ionic-transport behaviour of a given electrolyte was evaluated through equilibrium classical molecular dynamics simulations. The model with the scaled charges by 0.75 for charged ions was used to account for electronic screening and obtained converged conductivity and ionicity values. The transport coefficients (F_{ij}) and ionic conductivity (σ) were calculated using equations (5) and (6).

$$F_{ij} = \frac{1}{6}\lim_{t\to\infty}\frac{\mathrm{d}}{\mathrm{d}t}\left\langle \frac{1}{n_i}\sum_{\alpha}\left[r_{i,\alpha}(t) - r_{i,\alpha}(0)\right] \times \frac{1}{n_j}\sum_{\beta}\left[r_{i,\beta}(t) - r_{i,\beta}(0)\right]\right\rangle \quad (5)$$

$$\sigma = \frac{e^2}{Vk_BT} \sum_{i,j} z_i z_j n_i n_j F_{ij} \quad (6)$$

in which e is the electron charge, V is the volume of the simulation box, k_B is the Boltzmann constant and T is the temperature. i and j represent species and n_i (n_j) is the number of particles of species i (j). $r_{i,\alpha}$ is the displacement vectors for the motion of the αth particle of species i relative to the centre-of-mass position of the entire system[40,41].

AIMD calculations

AIMD simulations were performed using CP2K. We used the Perdew–Burke–Ernzerhof exchange-correlation functional, a GGA functional and the double-zeta valence polarized basis set and Goedecker–Teter–Hutter pseudopotentials. The efficient solution of the Poisson equation within the periodic boundary conditions is obtained in the reciprocal space by the expansion of the electronic density into a plane-wave basis set truncated at the energy cutoff of 400 Ry. The dispersion correction was applied in all calculations with the Grimme D3 method. Because of the large size of the cells, only the gamma point in the reciprocal space was used in our calculations. AIMD simulations were performed at 300 K with NVT ensembles and a time step of 1.0 fs. A stochastic velocity rescaling thermostat was used to control the temperature in AIMD simulations.

For simulations of Li^+ hopping transfer behaviour in bulk solvent, various solvent molecules with two Li^+ complexes were used in a periodic cubic box (column is calculated on the basis of density). A 20-ps simulation was performed to sample Li^+ transfer in bulk solvent. We extract the free energy of Li^+ hopping as:

$$\Delta E_{trans} = -k_B T \ln P \quad (7)$$

in which P is the probability as a function of Li–O (N) coordinate, T is temperature and k_B is the Boltzmann constant.

The anode consists of three layers of fully discharged graphite (LiC_6) with an armchair edge. Carbon armchair edges were functionalized with all oxygens. Two electrolyte systems, 1.3 M LiFSI/FAN (2 LiFSI and 40 FAN molecules) and 1.0 M $LiPF_6$/EC-EMC (2 $LiPF_6$, 8 EC and 12 EMC molecules) were evaluated. Initial geometries of the electrolyte were created with PACKMOL and then quenched using density functional forces. AIMD simulations were then performed at an elevated temperature of 350 K using a Nose thermostat to allow fast equilibration. At least 5 ps of dynamic simulations were performed for each system studied.

38. Kamaya, N. et al. A lithium superionic conductor. *Nat. Mater.* **10**, 682–686 (2011).
39. Hayashi, A., Hama, S., Morimoto, H., Tatsumisago, M. & Minami, T. Preparation of Li_2S–P_2S_5 amorphous solid electrolytes by mechanical milling. *J. Am. Ceram. Soc.* **84**, 477–479 (2001).
40. Fang, C., Mistry, A., Srinivasan, V., Balsara, N. P. & Wang, R. Elucidating the molecular origins of the transference number in battery electrolytes using computer simulations. *JACS Au* **3**, 306–315 (2023).
41. Fong, K. D., Self, J., McCloskey, B. D. & Persson, K. A. Onsager transport coefficients and transference numbers in polyelectrolyte solutions and polymerized ionic liquids. *Macromolecules* **53**, 9503–9512 (2020).

Acknowledgements This work is supported by the National Natural Science Foundation of China (22161142017, 22072134, U21A2081, 20727001, 91121020, 21327802, 21973102 and 22003071), the Natural Science Foundation of Zhejiang Province (LR23B030002 and LZ21B030002), and the Fundamental Research Funds for the Central Universities (2021FZZX001-09). M.M.R. and E.H. are supported by the Assistant Secretary for Energy Efficiency and Renewable Energy (EERE), the Vehicle Technologies Office (VTO) of the U.S. Department of Energy (DOE) through the Advanced Battery Materials Research (BMR) Program under contract no. DE-SC0012704. This research used beamline 23-ID-2 of the National Synchrotron Light Source II, a U.S. DOE Office of Science user facility operated for the DOE Office of Science by Brookhaven National Laboratory under contract number DE-SC0012704.

Author contributions D.L., R.L. and X.F. conceived the idea and designed the experiments. D.L., L.L., S.Y., Y.H., C.S., S.Z., H.Z. and J.Z. conducted the electrochemical experiments and characterizations, with the assistance of X.X., L.F., L.C. and X.F. M.M.R. performed XAS under the guidance of E.H. R.L. provided the theoretical calculations. P.Y. and J.W. performed the two-dimensional infrared spectroscopy test. D.L., T.D., J.W., E.H., C.W. and X.F. prepared the manuscript, with input from all the co-authors. All authors endorsed the final version of the manuscript.

Competing interests The authors declare no competing interests.

Additional information

Supplementary information The online version contains supplementary material available at https://doi.org/10.1038/s41586-024-07045-4.

Correspondence and requests for materials should be addressed to Enyuan Hu, Chunsheng Wang or Xiulin Fan.

Peer review information *Nature* thanks Chong Yan and the other, anonymous, reviewer(s) for their contribution to the peer review of this work.